

¹Department of Materials Science and Engineering, Southern University of Science and Technology, Shenzhen 518055, China; ²Advanced Technology Institute, Department of Electrical and Electronic Engineering, University of Surrey, Guildford GU2 7XH, UK; ³Clarendon Laboratory, Department of Physics, University of Oxford, Oxford OX1 3PU, UK; ⁴School of Physics and The University of Sydney Nano Institute, The University of Sydney, Sydney, NSW 2006, Australia; ⁵Future Photovoltaic Research Center, Global Institute of Future Technology, Shanghai Jiao Tong University, Shanghai 200240, China;

(Continued on next page)

MATERIALS SCIENCE

Dual molecular bridges at perovskite heterointerfaces for efficient inverted solar cells

Qing Lian^{1,†}, Lina Wang^{1,†}, Guoliang Wang^{1,4,†}, Guojun Mi^{1,†}, Bowei Li^{5,*}, Joel A. Smith³, Pietro Caprioglio³, Manuel Kober-Czerny³, Deng Wang¹, Qiming Yin¹, Jiong Yang⁶, Sibao Li⁷, Xiao Liang⁸, Shaokuan Gong⁷, Dongyang Li^{1,9}, Hanlin Hu⁸, Xihan Chen¹, Xugang Guo¹, Longbin Qiu⁷, Baomin Xu¹, Gang Li⁹, Anita W. Y. Ho-Baillie⁴, Wei Zhang^{2,10,*}, Guangfu Luo^{1,*}, Henry J. Snaith^{3,*} and Chun Cheng^{1,7,11,*}

ABSTRACT

Utilizing molecular bridges presents a promising means to enhance the performance of perovskite solar cells (PSCs). However, concurrently bridging the perovskite absorber and its two adjacent interfaces remains a significant challenge that is yet to be achieved. Here, we construct dual molecular bridges at perovskite heterointerfaces, enabled by a self-organizing additive of 4-fluoro-phenethylammonium formate (4-F-PEAFa) and a synthesized hole transporter of [2-(7H-dibenzo[c, g]carbazol-7-yl)ethyl]phosphonic acid (DBZ-2PACz). The molecular bridges spanning two interfaces lead to the formation of an ‘integral carrier transport pathway’, mitigating both non-radiative recombination and charge-transport losses in the fabricated PSC devices. We thus achieve a champion power conversion efficiency (PCE) of 26.0% (25.6% certified) in inverted PSCs, accompanied by an exceptionally high fill factor of 0.87 (maximum 0.88 from the certified devices, 97% of its Shockley–Queisser limit) and a low ideality factor of 1.06. The unencapsulated devices retain 96% of their PCEs after aging at 85°C for 2200 h and 90% after maximum power point tracking at an elevated temperature of 50°C for 973 h.

Keywords: perovskite solar cell, molecular bridge, heterointerface engineering, self-assemble material

INTRODUCTION

Considering the rapid growth of power conversion efficiencies (PCEs), e.g. from 3.9% in 2009 to 27.0% in 2025 [1,2], metal halide perovskite solar cells (PSCs) have shown great potential amongst the next-generation thin-film photovoltaics, in which the device normally consists of an n-i-p or p-i-n structure (also called inverted). Inverted PSCs (IPSCs) were first created in 2013 [3], standing out as promising contenders recently due to their fascinating attributes, such as simplified structure, low-temperature fabrication, excellent operational stability, diverse choices of charge transport materials, and compatibility with flexible substrates, multijunction cells and large-scale production [4–6]. However, most high-performance IPSCs (e.g. with certi-

fied PCEs >25%) still exhibit suboptimal fill factors (FFs, more details can be found in Table S1), primarily due to the interplay between charge recombination and extraction processes [7–12].

The continued advancement of PCE relies on substantial improvement in FF whilst concurrently upholding high open-circuit voltage (V_{OC}) and short-circuit current density (J_{SC}). This requires collective efforts to address the imperfect perovskite crystallization and the non-ideal adjacent interfaces, namely the buried interface between the perovskite and hole transport layer and the top interface between the perovskite and electron transport layer, both of which are closely linked with the notorious non-radiative recombination and charge-transport losses [13]. To tackle these challenges, perovskite

*Corresponding

authors. E-mails: bowei23@sjtu.edu.cn; wz0003@surrey.ac.uk; luogf@sustech.edu.cn; henry.snaith@physics.ox.ac.uk; chengc@sustech.edu.cn

[†]Equally contributed to this work.

[‡]Lead contact.

Received 23 December 2024;

Revised 20 March 2025; Accepted 21 May 2025

crystallization engineering and interface modifications are commonly implemented [14–18], including precise control of reaction kinetics [16,17] and the incorporation of multiple additives and treatments [18]. Despite their effectiveness in passivating defects and reducing recombination losses to enhance the V_{OC} , these techniques often fail to leverage this passivation effect for improved charge extraction. Additionally, while such approaches could provide a modest improvement in FF, they are insufficient to mitigate charge-transport losses due to the inevitable increase in contact resistance. Recent studies indicate that constructing carrier viaducts through molecular bridging is an efficient strategy for charge extraction and transport [19,20]. However, this approach is largely confined to improving an individual functional layer or specific interface instead of the entire device. Thus, it is imperative to develop a holistic approach to enable the fabrication of high-performance IPSCs with excellent reproducibility and long-term stability.

In this study, we construct dual molecular bridges at perovskite adjacent heterointerfaces through the combination of the additive (4-fluorophenethylammonium formate, 4-F-PEAFa) and hole transporter ([2-(7H-dibenzo[c, g]carbazol-7-yl)ethyl]phosphonic acid, DBZ-2PACz). This strategy enables the comprehensive regulation of perovskite absorber and its adjacent interfaces, resulting in both low non-radiative recombination losses and carrier transport losses. Based on a series of theoretical and experimental characterizations, we demonstrate that 4-F-PEAFa can spontaneously distribute throughout the as-crystallized perovskite film, increasing the grain size, charge carrier mobilities, and quasi-Fermi level splitting when in contact with both charge transport layers. Thanks to the self-organizing characteristic, 4-F-PEAFa firmly bonds with the perovskite surface and bridge both the bottom hole transporter and top electron transporter, leading to the formation of ‘dual molecular bridges’ throughout IPSC devices. This integral carrier transport pathway enhances carrier extraction/transport and thus substantially increases the device FF. Coupled with our synthesized DBZ-2PACz hole transporter, we realize IPSCs with a certified champion PCE of 25.6% and FF of 0.87 (with a certified maximum of 0.88 and a low ideality factor of 1.06), approaching its Shockley–Queisser limit at the corresponding bandgap. Encouragingly, the long-term stability of devices has shown significant improvement under three different levels of the international Summit on Organic Photovoltaic Stability (ISOS) protocols, including ISOS-D-1, ISOS-D-2I, and ISOS-L-2I testing.

RESULTS AND DISCUSSION

Holistic construction of molecular bridges

We proposed the construction of dual molecular bridges at perovskite heterointerfaces based on the following considerations: (1) The additive with anchoring groups could function as bridges, with tight bonding to perovskite film and stretching out to interact with the adjacent charge transporters [20,21]. (2) The tailored design of charge transport materials could enhance the interaction with the extended functional groups of the additive, thereby optimizing interfacial properties [22]. (3) The constructed molecular bridges could offer additional benefits, such as improved perovskite crystallization, defect passivation, and energy level alignment [19,20]. These concepts are illustrated in Fig. 1A. Therefore, we first start screening perovskite additives from 12 fluorinated organic salts (n -F-PEAX, $n = 2, 3$ and 4; $X = I^-, Br^-, Cl^-$, and $HCOO^-$, Fig. 1B). These additives were systematically assessed by density functional theory (DFT) calculations (Note S1) [23]. The fluorinated cations (2-F-PEA $^+$, 3-F-PEA $^+$, and 4-F-PEA $^+$) possess a smaller size of NH_3^+ when compared to FA $^+$, leading to stronger adsorption with the PbI_2 subsurface layer and more stable n -F-PEAI-terminated surfaces of the perovskite (Fig. S1, Video S1). Figure 1C shows higher formation energies (E_f) of iodide vacancies (V_I) on n -F-PEAI-terminated surfaces (2.06–2.35 eV vs 1.90 eV for a pristine FAI-terminated surface), in which the maximum E_f suggests the fewest V_I on the 4-F-PEAI-terminated surface. It is noteworthy that the dipole moment of n -F-PEA increases with n and exhibits a strong linear relationship with its dimerization energy and the V_I formation energy on the n -F-PEAI-termination surface (Table S2 and Fig. S2). This phenomenon can be explained by the fact that a greater dipole moment leads to a more polarizable electron cloud, thereby strengthening van der Waals interactions and contributing to a more stable surface. Because the FAI-terminated surface is expected to be the dominant one in experiments [24], we further examine the passivation of iodide vacancies in the FAI-terminated surface by $HCOO^-$ and different halide anions (Cl^- , Br^- , I^-). The binding energies (E_b) between the surface V_I and I^- , Br^- , Cl^- , $HCOO^-$ were determined to be -2.58 , -2.84 , -3.13 , and -3.20 eV, respectively (Fig. 1D). Amongst them, $HCOO^-$ exhibits the strongest binding with surface V_I . Other defects in the minor PbI_2 -terminated surface [25], such as Pb_I antisites and FA interstitials can also be efficiently passivated by $HCOO^-$ (Fig. S3). Therefore, the 4-F-PEACOOH (abbreviated as

(Continued from previous page)

⁶Department of Chemistry, Southern University of Science and Technology, Shenzhen 518055, China; ⁷SUSTech Energy Institute for Carbon Neutrality, Department of Mechanical and Energy Engineering, Southern University of Science and Technology, Shenzhen 518055, China;

⁸Hoffman Institute of Advanced Materials, Shenzhen Polytechnic, Shenzhen 518055, China; ⁹Department of Electronic and Information Engineering, Research Institute for Smart Energy, The Hong Kong Polytechnic University, Hong Kong 999077, China;

¹⁰State Centre for International Cooperation on Designer Low-carbon & Environmental Materials (CDLCEM), School of Materials Science and Engineering, Zhengzhou University, Zhengzhou 450001, China and

¹¹Guangdong Provincial Key Laboratory of Energy Materials for Electric Power, Southern University of Science and Technology, Shenzhen 518055, China

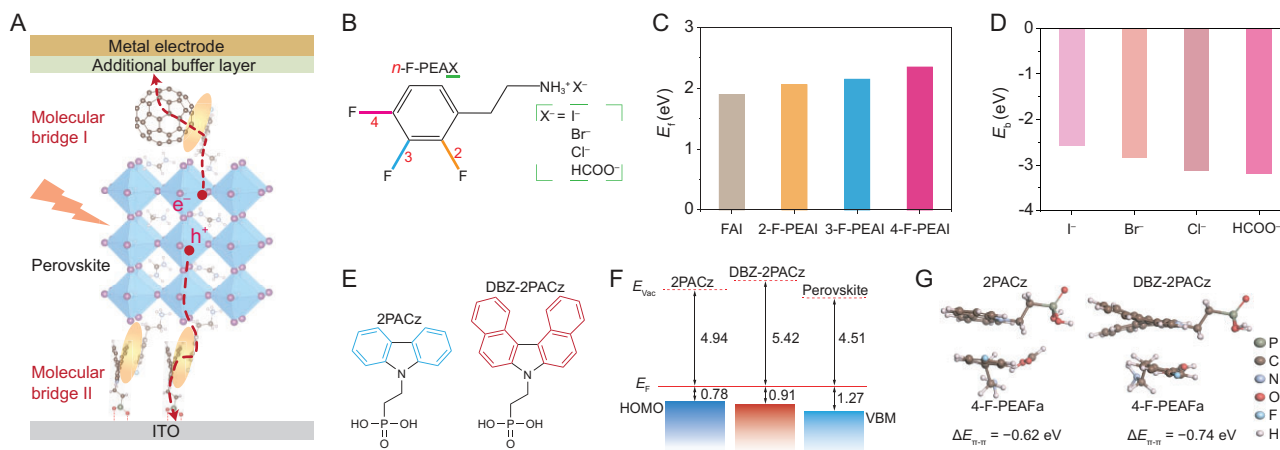


Figure 1. Construction of molecular bridges at perovskite adjacent interfaces. (A) Schematic of the proposed approach in the entire device. The yellow ellipse and red dash lines represent the interaction and the carrier pathway, respectively. (B) Cation and anion engineering of *n*-F-PEAX. '*n*' denotes the substitutional position of the fluorine, and 'X' represents anions, I⁻, Br⁻, Cl⁻, and HCOO⁻. (C) Formation energy (E_f) of iodide vacancy (V_i) in different surfaces. (D) Binding energy (E_b) between the V_i in the FAI-terminated surface of $\text{Cs}_{0.05}\text{FA}_{0.85}\text{MA}_{0.1}\text{PbI}_{2.9}\text{Br}_{0.1}$ (Cs, cesium; FA, formamidinium; MA, methylammonium) and various anions. (E) Structure of 2PACz and DBZ-2PACz. (F) Band edge positions extracted from UPS measurements. E_{vac} is vacuum level, E_F is Fermi level, HOMO is the highest occupied molecular orbital, and VBM is the valence band maximum. (G) DFT-predicted π - π interaction between 4-F-PEAFa and 2PACz or DBZ-2PACz. The side view is shown here and the inset values denote the binding energy.

4-F-PEAFa in the following sections) demonstrated an optimal combination of cation and anion in these fluorinated organic salts (evidenced in Figs S4 and S5). To link the perovskite layer and the carrier transport layers, the incorporation of phenyl units within the perovskite additive of 4-F-PEAFa and the selection of compatible carrier transport materials are imperative. The 4-F-PEA⁺ cations absorbed on perovskite surfaces have the capability to extend and establish a connection with the adjacent carrier transporters. Consequently, molecular bridges can be constructed. Molecular bridge I significantly facilitates electron transport (Fig. S6), due to the strong interaction between 4-F-PEA⁺ and C₆₀ (Fig. S7) and the firm adsorption of 4-F-PEA⁺ to perovskite.

Then, we initiated the optimization process for the hole transport materials. We synthesized a derivative of the 2-(9H-carbazol-9-yl)ethyl]phosphonic acid (2PACz), namely [2-(7H-dibenzo[*c, g*]carbazol-7-yl)ethyl]phosphonic acid (DBZ-2PACz [26], Fig. 1E, Fig. S8) as a more adapted hole transporter for the construction of molecular bridge II. It is noted that these two molecules are considered due to the phenyl units that can form π - π interactions with the addition of 4-F-PEAFa and the group of phosphonic acids that can be fixed to the ITO surface. Herein, DBZ-2PACz has a deeper band edge (0.91 eV) as compared to 2PACz (0.78 eV) (Fig. 1F, Fig. S9). This reduced energy offset when in contact with the perovskite contributes to the enhanced V_{OC} and FF in our fabricated devices (Fig. S10). Furthermore, DFT results indicate a stronger interaction between 4-F-PEAFa

and DBZ-2PACz ($\Delta E_{\pi-\pi} = -0.74$ eV) than 2PACz ($\Delta E_{\pi-\pi} = -0.62$ eV) (Fig. 1G, Fig. S11). Enabled by such a stronger π - π interaction, 4-F-PEAFa can well bridge the hole transporter and perovskite at the buried interface, which could lead to a significant reduction in both non-radiative recombination losses and carrier transport losses at this interface, as verified by the time-resolved photoluminescence (TRPL) measurements [27] (Fig. S12). These characteristics reaffirm the advantages and effectiveness of constructing molecular bridge II.

The existence of molecular bridges at perovskite interfaces can be further investigated by X-ray photoelectron spectroscopy (XPS) and X-ray diffraction (XRD). As shown in Fig. S13, the mixed thin films of 4-F-PEAFa/DBZ-2PACz and 4-F-PEAFa/C₆₀ exhibit a stronger $\pi \rightarrow \pi^*$ shakeup satellite compared to individual components in C1s XPS spectra. Additionally, when mixed with DBZ-2PACz, certain peak intensities of 4-F-PEAFa show a significant decrease in XRD patterns (Fig. S14), suggesting an interaction between 4-F-PEAFa and DBZ-2PACz. These findings confirmed the significant π - π interactions between 4-F-PEAFa and C₆₀ or DBZ-2PACz transporters, leading to the formation of the molecular bridges. Furthermore, 4-F-PEAFa can affect the energy level of the perovskite (Figs S15 and S16), leading to different band positions at both buried and top interface. At the buried interface contacting DBZ-2PACz, the higher valence band maximum (VBM) indicated a facilitated hole transfer thanks to the reduced energy offset, consistent with Fig. 1F. At the top surface, 4-F-PEAFa induced a deeper VBM,

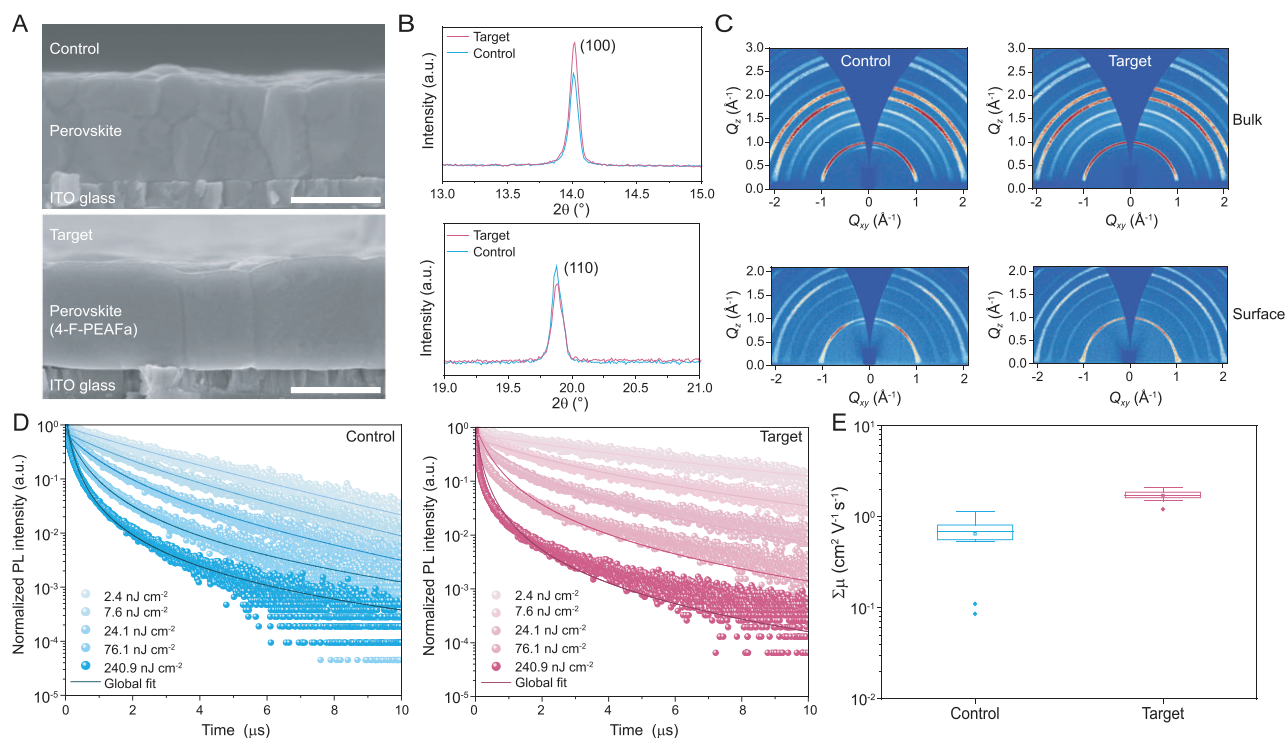


Figure 2. Characterization of perovskite films with or without adding 4-F-PEAFa. (A) Cross-sectional SEM images. The scale bars are 500 nm. (B) Enlarged XRD patterns. All films were deposited on the DBZ-2PACz-coated ITO glass. (C) 2D GIWAXS patterns for control and target films, measured at incidence angles $\alpha_i = 0.5^\circ$ for ‘surface’ measurements and $= 2^\circ$ for ‘bulk’ measurements, corresponding to attenuation lengths of 73 nm and 345 nm, respectively. (D) Fluence-dependent TRPL decays incident from the quartz side excited at 398 nm. Note that the perovskite films were deposited on the quartz. (E) Sum of charge carrier mobility of perovskite films obtained from the TPC measurements. Twelve data points from 2 samples at 6 different laser fluences were collected for each condition.

which can act as a hole blocking effect [3]. These characteristics enable improved charge transport and reduced recombination losses at both perovskite heterointerfaces.

Characterizations of perovskite films

To confirm the functions of 4-F-PEAFa, we conducted a range of characterizations based on the as-prepared perovskite films (referred to as ‘control’) and those with the additive (referred to as ‘target’). Compared to the control film, the target film with a compact and uniform morphology has shown larger grain sizes (see the top-view scanning electron microscopy (SEM) in Fig. S17, Note S2). Cross-sectional SEM images (Fig. 2A) show a monolithic grain structure extending throughout the entire film (600–650 nm). XRD patterns of the target film exhibit a higher intensity along the [100] direction or (100) plane and an enhanced ratio of (100)/(110) (1.38 vs 0.84, obtained from the integrated peak intensity) (Fig. 2B, Fig. S18). Grazing-incidence wide-angle X-ray scattering (GIWAXS) measurements confirm that the target film has reduced (110) intensity and increased (100) intensity in the out-of-plane direction (Fig. 2C). Additionally,

the target film exhibits a reduced monomolecular recombination rate constant (k_1 , from 0.9×10^5 to $0.5 \times 10^5 \text{ s}^{-1}$, Note S3) as determined by the TRPL measurements (Fig. 2D), and improved long-range charge carrier mobilities (sum-of-mobility of electron and hole, $\Sigma\mu$, from 0.65 to $1.71 \text{ cm}^2 \text{ V}^{-1} \text{ s}^{-1}$, Note S4) as confirmed by transient photoconductivity (TPC) measurements (Fig. 2E). These gains in carrier dynamic characteristics could be attributed to the enhanced crystallinity of the target film as revealed above [28,29].

Modification of 4-F-PEAFa on perovskite heterointerfaces

We further performed time-of-flight secondary-ion mass spectrometry (ToF-SIMS) to detect the distribution of 4-F-PEAFa in the target film as shown in Fig. 3A. The positive ions of Pb^{2+} and In^+ denote the spatial location of perovskite and indium tin oxide (ITO) glass, respectively, whereas the negative ions of F^- and HCOO^- can be used to trace the 4-F-PEAFa. Interestingly, the F^- has a bimodal distribution, accumulating on both top (also confirmed in Fig. S19) and buried interfaces, whilst the HCOO^- is mainly located at the buried interface. We assume

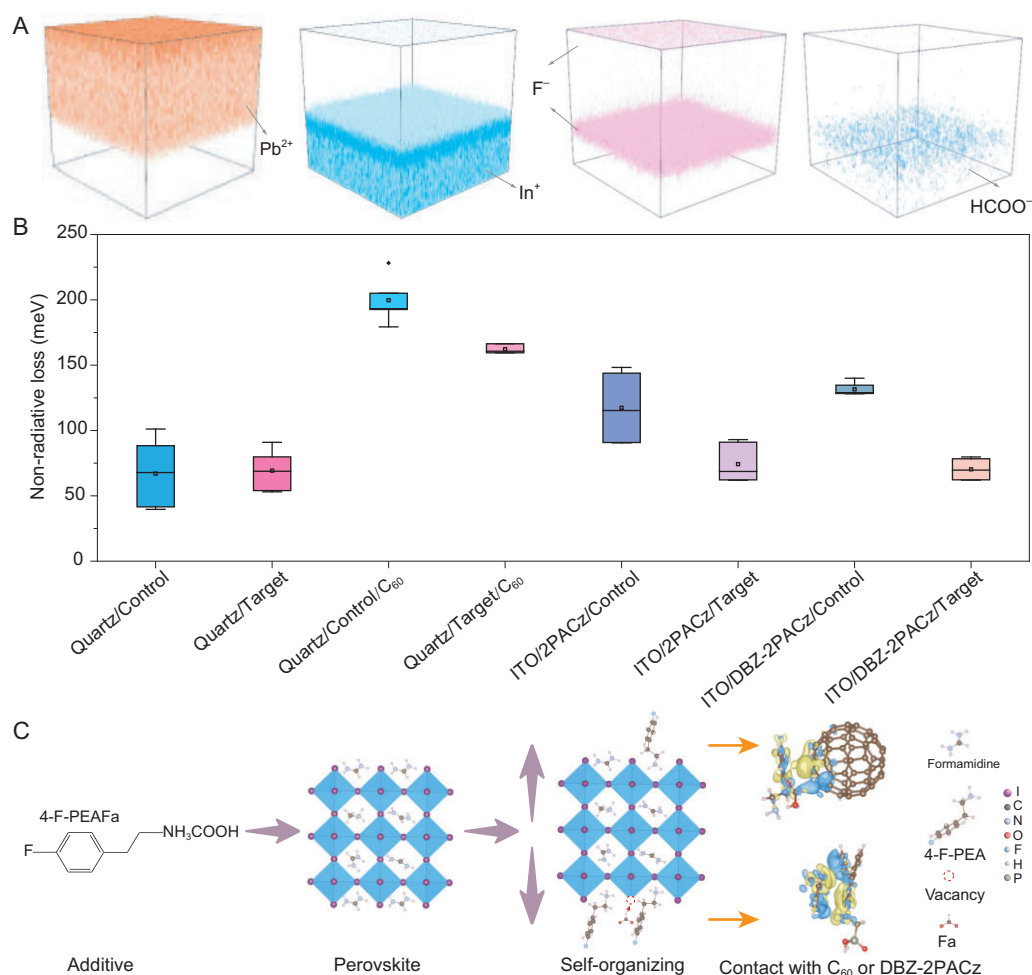


Figure 3. Self-organizing 4-F-PEAFa and its effect on perovskite with or without contacting charge transporters. (A) 3D depth profiles of ion distributions obtained from the ToF-SIMS measurements. (B) Non-radiative losses of perovskite films on different types of substrates or contacts. (C) Illustration of the self-organizing phenomenon of 4-F-PEAFa and the charge density difference. The red color circle (dash line) denotes the iodide vacancy and the Fa is prone to occupy this position. The 4-F-PEA occupies the FA at the dual sides of the perovskite. The blue regions represent electron accumulation, while the yellow regions indicate electron loss.

this phenomenon is caused by the species' properties. A small amount residing near the top surface could be ascribed to the large size of 4-F-PEA⁺ [30], which cannot enter the perovskite structure and will thus stay at the surface during initial nucleation (see details in Fig. S20). The pseudohalide HCOO⁻ could alter the Pb coordination environment and thus the perovskite crystallization [21]. Hence, it is more likely to aggregate near the bottom given the top-down growth of the antisolvent-assisted spin-coated perovskite film [31]. To gain insight into this phenomenon, we calculated the dissociation energy for each organic salt component in the solution and found that 4-F-PEAFa is supposed to retard the perovskite crystallization by forming stable 4-F-PEAI and Pb(HCOO)₂ with respect to FAI and PbI₂ (Table S3). Therefore, 4-F-PEAFa shows spontaneous distribution or 'self-organizing' at both interfaces.

To understand the effects of such a self-organizing additive, we studied the carrier dynamics of the perovskite films under different conditions. When the perovskite is in contact with charge transporters, a reduction of photoluminescence quantum yield (PLQY) is observed (Fig. S21). This is consistent with interfacial recombination as previously reported [32]. Encouragingly, with the incorporation of 4-F-PEAFa in perovskite film, the PLQY at both interfaces are substantially recovered. The calculated quasi-Fermi level splitting (QFLS, Figs S22 and S23, Note S5) and non-radiative losses (Fig. 3B, Note S6) confirm a reduction of non-radiative recombination at both heterointerfaces. Hence, the 4-F-PEAFa not only modifies the perovskite bulk but also plays a significant function at perovskite heterointerfaces. These effects are closely related to the spatial regulation of 4-F-PEAFa. Specifically, at the buried interface, the accumulation of 4-F-PEA⁺ and

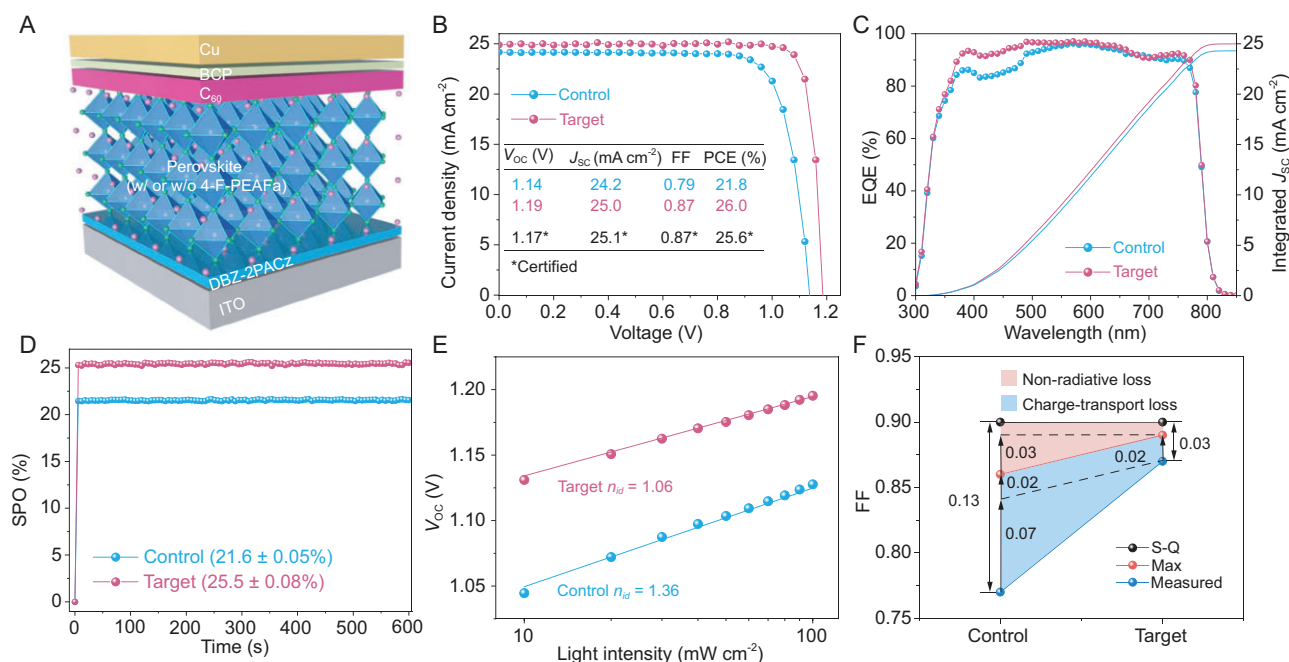


Figure 4. Characterizations of unencapsulated IPSCs with or without adding 4-F-PEAFa. (A) Schematic configuration of the device. (B) Champion current density-voltage (J - V) curves under AM 1.5 G simulated solar illumination. (C) EQE spectra. (D) Stabilized power output (SPO) determined at V_{MPP} . For SPO, the devices were measured under the AAA solar simulator (Xenon lamp, without UV filter). The V_{MPP} of the control and target is 0.95 and 1.06 V, respectively. (E) Light intensity dependency of V_{oc} . The ideality factor (n_{id}) is obtained from the linear fit. (F) The analysis of the FF losses, including the Shockley–Queisser (S-Q), maximum (max) and measured FF. All calculation details can be found in the Supplementary materials. The blue area denotes the charge-transport loss and the pink area denotes the non-radiative loss. The dashed lines help to indicate the reduced FF losses.

HCOO^- enable the suppression of perovskite defects as we discussed earlier in the DFT calculations, thereby effectively reducing interfacial losses. At the top interface, the large organic 4-F- PEA^+ does not form a 2D phase, with no detectable scattering ring in 2D GIWAXS patterns (Fig. 2C) or peaks in the 1D integrated data (Fig. S24). Nonetheless, the π -conjugation structure of 4-F- PEA^+ leads to good stacking with the C_{60} (Fig. S7), facilitating electron transport between the perovskite layer and the top electrodes (Fig. S6). Therefore, the terminal groups of 4-F- PEA^+ provide favourable connection with both the C_{60} and DBZ-2PACz to achieve dual molecular bridges. This will lead to the development of an efficient integral carrier transport pathway throughout the entire device. Further calculated charge density difference indicated the charge transfer at both perovskite heterointerfaces (Fig. 3C), which could be beneficial for the performance of the device.

Photovoltaic performance

To verify the effects of molecular bridges, we fabricated >700 devices with a structure of glass/ITO/DBZ-2PACz/perovskite/ C_{60} /bathocuproine (BCP)/Cu (Fig. 4A, Fig. S25). The presence of DBZ-2PACz in IPSCs as the hole

transporter was detected in the depth profile (Fig. S26). Statistical data (Fig. S27) confirmed a remarkable performance improvement between the control (without 4-F-PEAFa) and target devices (with 4-F-PEAFa) and excellent repeatability, in which the champion efficiency increased from 21.8% to 26.0% and the champion FF increased from 0.83 to 0.87 (Fig. 4B). Compared to the control devices, our target devices exhibit improved homogeneity, as observed in the statistical data. Such high uniformity is crucial for the industrialization of perovskite photovoltaics, directly impacting large-scale reproducibility and commercial viability. The significant enhancement in homogeneity can be attributed to the incorporation of dual molecular bridges. Our modifications to perovskite adjacent interfaces resulted in more uniform carrier extraction and reduced local defects, leading to lower device-to-device variability, which is critical for large-area scalability (Fig. S28).

To verify the photovoltaic parameters measured in our lab, we sent five high-performing devices to an accredited laboratory for certification. The champion performance yields a V_{oc} of 1.17 V, a J_{sc} of 25.1 mA cm^{-2} , an FF of 0.87 and a PCE of 25.6% in the reverse scan; a V_{oc} of 1.17 V, a J_{sc} of 25.1 mA cm^{-2} , an FF of 0.86 and a PCE of 25.2% in the forward scan (Fig. S29). These devices reached an average PCE of 25.1% ($25.1 \pm 0.35\%$, obtained

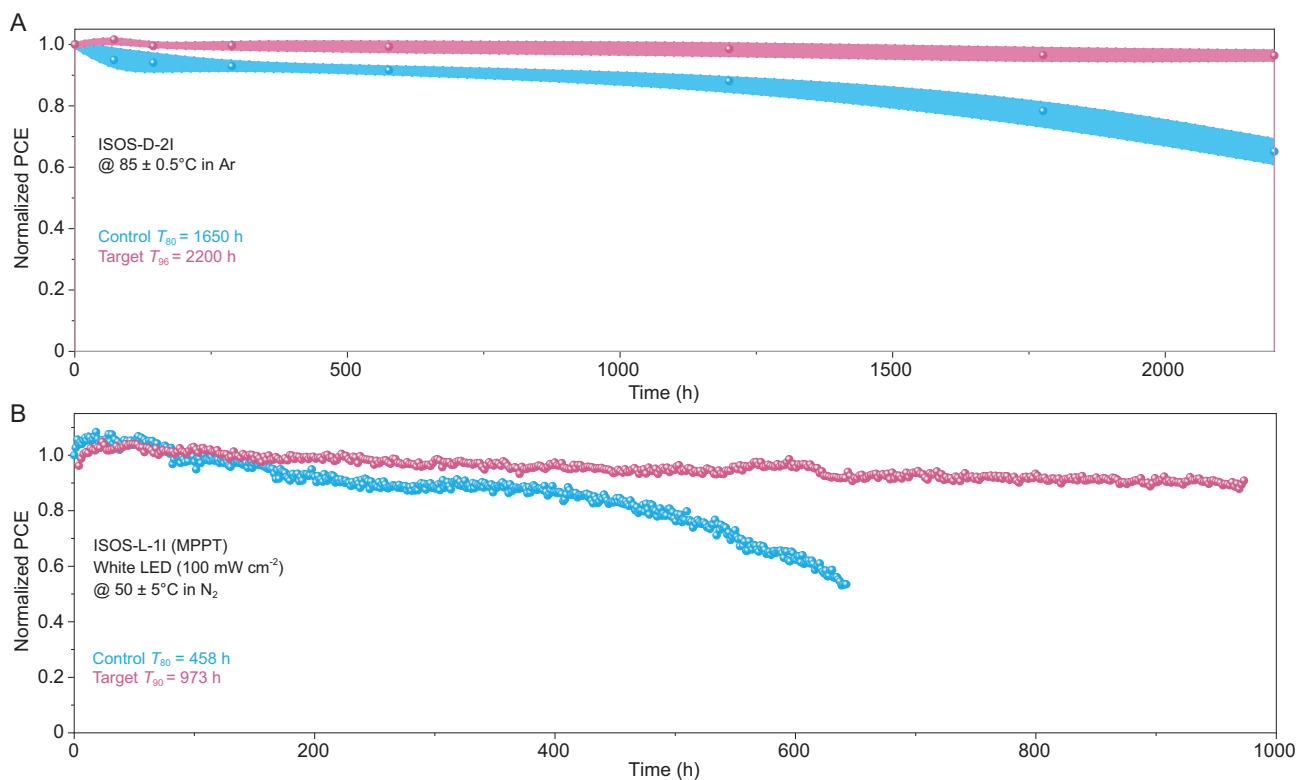


Figure 5. Long-term stability under (A) thermal or (B) maximum power point tracking. Note that five devices for each group were measured for thermal stability. The width of the shaded regions represents the standard deviation of the PCEs.

from both forward and reverse scans in Table S4). To the best of our knowledge, the certified PCE of 25.6% and FF of 0.87 (96% of its Shockley–Queisser limit for a PSC with a 1.57 eV bandgap) achieved in this study are amongst the highest photovoltaic parameters reported to date (see more details in Table S1 and Fig. 4B). Additionally, such certified high FF (the maximum is 0.88, with an average of 0.87 ± 0.01 in Table S4) and the product of $V_{OC} \times FF$ (88% of the Shockley–Queisser limit) indicate an extremely efficient collection of photo-generated carriers from the perovskite into the charge transport layers [14].

We calculated the integrated J_{SC} from external quantum efficiency (EQE) spectra where the control and target device show 24.3 mA cm^{-2} and 25.0 mA cm^{-2} , respectively (Fig. 4C), with a negligible mismatch between the J - V and EQE measurements. Figure 4D shows the steady-state power output (SPO) at the maximum power point voltage (V_{MPP}). The steady-state PCEs ($21.6\% \pm 0.05\%$ for the control and $25.5\% \pm 0.08\%$ for the target) closely match the J - V scan-determined PCEs. Compared to the control, the target device shows a reduced voltage deficit (defined by $E_g/q - V_{OC}$, where E_g is the bandgap, 1.57 eV from Fig. S30) from 0.43 to 0.38 V. More significantly, light-intensity dependent V_{OC} measurements exhibit a suppressed ideality

factor ($n_{id} = 1.06$ for the target device, Fig. 4E and Fig. S31), which is the lowest value among the high-performance PSCs (Table S1). Both characteristics demonstrate high perovskite quality and minimal interfacial losses [33].

It is known that the FF can be affected by the sweep direction due to hysteresis in J - V curves. Here, both statistical lab-measured (Fig. S27) and certified (Fig. S29, Table S4) data show the stable variation of the FF either from forward or reverse scans, making them ideal candidates for quantitative analyses. To understand the FF improvement, n_{id} values and the corresponding J - V data were further exploited. The maximum FFs (without considering resistance) of the control and target devices are 0.86 and 0.89 (Fig. 4F, Note S7), approaching the Shockley–Queisser limit value of 0.903 at a 1.57 eV band gap. After introducing the equivalent series (control vs target, 3.57 vs $1.41 \text{ Ohm}\cdot\text{cm}^2$) and shunt resistances (6840 vs $10\,602 \text{ Ohm}\cdot\text{cm}^2$), the calculated FFs (0.79 vs 0.86) are in good agreement with the measured FFs (0.77 vs 0.87) for the control and target devices. In comparison with the reduced non-radiative losses of 0.03, the charge-transport losses are significantly inhibited by 0.07 in the target device. This phenomenon could be attributed to the properties of the top-down carrier viaduct, which

relies on two molecular bridges positioned on both sides of the perovskite layer. The total FF loss significantly decreased from 0.13 to 0.03, demonstrating the effectiveness of the approach in this study.

Long-term stability

We further investigated the long-term performance stability of our devices without any encapsulation under three conditions based on the International Summit on Organic Photovoltaic Stability (ISOS) protocols [34]. In ISOS-D-1 testing (Fig. S32), the T_{85} (lifetime at 85% of the initial efficiency) of devices is enhanced from 271 to 1128 h with 4-F-PEAFa modification. This may be related to improved robustness to moisture, with contact angle measurements confirming a more hydrophobic surface of the 4-F-PEAFa-containing perovskite (Fig. S33). Furthermore, over 2200-h ISOS-D-2I testing (Fig. 5A), the target devices show better thermal resistance with a T_{96} (lifetime at 96% of the initial efficiency) of 2200 h. In contrast, the control devices only retain a T_{80} (lifetime at 80% of the initial efficiency) of 1650 h. Determined at maximum power point (Fig. 5B), the ISOS-L-2I tracking shows a T_{80} of 458 h for the control device and a T_{90} of 973 h for the target device. This enhanced operational stability could be ascribed to the passivation effect of the molecular bridges at adjacent interfaces, which are beneficial for inhibiting ion migration under heat or light stressors [5]. Taken together, the results demonstrate that our rationally designed molecular bridges at perovskite adjacent heterointerfaces simultaneously improved the photovoltaic performance and stability of IPSCs.

CONCLUSIONS

In this work, we successfully construct dual bridges at perovskite heterointerfaces through the addition of 4-F-PEAFa, which can be firmly absorbed on the perovskite surface and interacts with the electron transporter (C_{60}) at the top interface and synergistically links with a customized hole transporter (DBZ-2PACz) at the bottom interface. Such a molecular design approach contributes to reduction of non-radiative recombination and charge-transport losses at perovskite heterointerfaces through the formation of an efficient carrier transport pathway in the complete devices, resulting in inverted perovskite solar cells with a certified efficiency of 25.6% and an exceptional fill factor of 0.87, along with excellent thermal and operational stability. Our study highlights the significance of the integral design of molecular bridges and provides useful guidance in the commercialization of these promising photovoltaic devices.

DATA AVAILABILITY

The datasets generated during and/or analyzed during the current study are available from the corresponding author on reasonable request.

SUPPLEMENTARY DATA

Supplementary data are available at [NSR](#) online.

ACKNOWLEDGEMENTS

We thank Kai Wang from the Southern University of Science and Technology for photoelectronic measurements, Steven Hinder from the University of Surrey (UK) for his kind suggestion of ToF-SIMS, and Yao Wu from the University of Surrey (UK) for Jamovi training and data analysis. All the DFT calculations were carried out on the Taiyi cluster supported by the Center for Computational Science and Engineering of Southern University of Science and Technology.

FUNDING

This work was supported by the Basic Research Project of Science and Technology Plan of Shenzhen (20231115112954001), the High Level of Special Funds (G03034K001), the Guangdong Science and Technology Fund (2018B030322001). Q.L. thanks the National Natural Science Foundation of China (22305111). B.X. thanks the National Key Research and Development Project Funding from the Ministry of Science and Technology of China (2021YFB3800101). X.G. is grateful for financial support from the National Natural Science Foundation of China (52173171). W.Z. thanks EPSRC standard research (EP/V027131/1) for financial support. L.W. and G.L. were supported by the Introduced Innovative R&D Team of Guangdong (2017ZT07C062) and the Shenzhen Science and Technology Innovation Commission (JCYJ20200109141412308). B.L. thanks the Startup Fund for Young Faculty at SJTU (SFYFat SJTU, 24 X 010502888), the National Natural Science Foundation of China (22409130) and the Shanghai Science and Technology Innovation Action Plan (24DZ3001203).

AUTHOR CONTRIBUTIONS

Q.L., G.W. and C.C. conceived the idea. W.Z., G.L., H.J.S. and C.C. supervised the projects. L.W. carried out DFT calculations under the supervision of G.L. B.L. wrote the draft of the manuscript. Q.L. conducted material design, synthesis and device fabrication. Q.L., G.W. and J.Y. designed and synthesized SAMs. G.W., D.W. and S.L. assisted in device fabrication, anti-reflection layer and stability testing. J.A.S., X.L. and H.H. carried out GIWAXS measurements and data analysis. P.C. carried out PLQY measurements and analysis. M.K.-C. carried out the TRPL, TPC and mobility measurements. J.Y. carried out XPS and UPS measurements. S.G. and X.C. contributed to photoelectronic measurements and analysis. D.L. and G.L. carried out ToF-SIMS measurements and data analysis. X.G. and B.X. supported essential equipment and funding. All authors discussed the results and contributed to the manuscript revisions.

Conflict of interest statement. H.J.S. is a co-founder, chief scientific officer, and director of Oxford PV Ltd.

REFERENCES

- Kojima A, Teshima K, Shirai Y *et al.* Organometal halide perovskites as visible-light sensitizers for photovoltaic cells. *J Am Chem Soc* 2009; **131**: 6050–1.
- National Renewable Energy Laboratory (NREL). *Best Research-Cell Efficiency Chart*. <https://www.nrel.gov/pv/assets/pdfs/best-research-cell-efficiencies.pdf> (21 April 2025, date last accessed).
- Jeng J, Chiang Y, Lee M *et al.* CH₃NH₃PbI₃ perovskite/fullerene planar-heterojunction hybrid solar cells. *Adv Mater* 2013; **25**: 3727–32.
- Lin Y, Sakai N, Da P *et al.* A piperidinium salt stabilizes efficient metal-halide perovskite solar cells. *Science* 2020; **369**: 96–102.
- Azmi R, Ugur E, Seitkhan A *et al.* Damp heat-stable perovskite solar cells with tailored-dimensionality 2D/3D heterojunctions. *Science* 2022; **376**: 73–7.
- Li B and Zhang W. Improving the stability of inverted perovskite solar cells towards commercialization. *Commun Mater* 2022; **3**: 65.
- Jiang Q, Tong J, Xian Y *et al.* Surface reaction for efficient and stable inverted perovskite solar cells. *Nature* 2022; **611**: 278–83.
- Zhang S, Ye F, Wang X *et al.* Minimizing buried interfacial defects for efficient inverted perovskite solar cells. *Science* 2023; **380**: 404–9.
- Tan Q, Li Z, Luo G *et al.* Inverted perovskite solar cells using dimethylacridine-based dopants. *Nature* 2023; **620**: 545–51.
- Chen P, Xiao Y, Hu J *et al.* Multifunctional ytterbium oxide buffer for perovskite solar cells. *Nature* 2024; **625**: 516–22.
- Chen H, Liu C, Xu J *et al.* Improved charge extraction in inverted perovskite solar cells with dual-site-binding ligands. *Science* 2024; **384**: 189–93.
- Cao Q, Li Y, Zhang H *et al.* Efficient and stable inverted perovskite solar cells with very high fill factors via incorporation of star-shaped polymer. *Sci Adv* 2021; **7**: eabg0633.
- Stolterfoht M, Wolff CM, Márquez JA *et al.* Visualization and suppression of interfacial recombination for high-efficiency large-area pin perovskite solar cells. *Nat Energy* 2018; **3**: 847–54.
- Peng W, Mao K, Cai F *et al.* Reducing nonradiative recombination in perovskite solar cells with a porous insulator contact. *Science* 2023; **379**: 683–90.
- Li C, Wang X, Bi E *et al.* Rational design of Lewis base molecules for stable and efficient inverted perovskite solar cells. *Science* 2023; **379**: 690–4.
- Yang S, Chen S, Mosconi E *et al.* Stabilizing halide perovskite surfaces for solar cell operation with wide-bandgap lead oxysalts. *Science* 2019; **365**: 473–8.
- Li X, Zhang W, Guo X *et al.* Constructing heterojunctions by surface sulfidation for efficient inverted perovskite solar cells. *Science* 2022; **375**: 434–7.
- Degani M, An Q, Albaladejo-Siguan M *et al.* 23.7% efficient inverted perovskite solar cells by dual interfacial modification. *Sci Adv* 2021; **7**: eabj7930.
- Zhou Q, Qiu J, Wang Y *et al.* Multifunctional chemical bridge and defect passivation for highly efficient inverted perovskite solar cells. *ACS Energy Lett* 2021; **6**: 1596–606.
- Xu H, Liang Z, Ye J *et al.* Constructing robust heterointerfaces for carrier viaduct via interfacial molecular bridges enables efficient and stable inverted perovskite solar cells. *Energy Environ Sci* 2023; **16**: 5792–804.
- Jeong J, Kim M, Seo J *et al.* Pseudo-halide anion engineering for α -FAPbI₃ perovskite solar cells. *Nature* 2021; **592**: 381–5.
- He R, Wang W, Yi Z *et al.* Improving interface quality for 1-cm² all-perovskite tandem solar cells. *Nature* 2023; **618**: 80–6.
- Lin R, Xu J, Wei M *et al.* All-perovskite tandem solar cells with improved grain surface passivation. *Nature* 2022; **603**: 73–8.
- Brinck S and Infante I. Surface termination, morphology, and bright photoluminescence of cesium lead halide perovskite nanocrystals. *ACS Energy Lett* 2016; **1**: 1266–72.
- Oner SM, Sezen E, Yordanli MS *et al.* Surface defect formation and passivation in formamidinium lead triiodide (FAPbI₃) perovskite solar cell absorbers. *J Phys Chem Lett* 2022; **13**: 324–30.
- Li B, Zhang C, Gao D *et al.* Suppressing oxidation at perovskite-NiO interface for efficient and stable tin perovskite solar cells. *Adv Mater* 2024; **36**: 2309768.
- Zheng X, Chen B, Dai J *et al.* Defect passivation in hybrid perovskite solar cells using quaternary ammonium halide anions and cations. *Nat Energy* 2017; **2**: 17102.
- Ma C, Kang M-C, Lee S-H *et al.* Photovoltaically top-performing perovskite crystal facets. *Joule* 2022; **6**: 2626–43.
- Luo C, Zheng G, Gao F *et al.* Facet orientation tailoring via 2D-seed-induced growth enables highly efficient and stable perovskite solar cells. *Joule* 2022; **6**: 240–57.
- Lee J, Tan S, Seok S *et al.* Rethinking the A cation in halide perovskites. *Science* 2022; **375**: eabj1186.
- Chen S, Xiao X, Chen B *et al.* Crystallization in one-step solution deposition of perovskite films: upward or downward? *Sci Adv* 2021; **7**: eabb2412.
- Stolterfoht M, Caprioglio P, Wolff CM *et al.* The impact of energy alignment and interfacial recombination on the internal and external open-circuit voltage of perovskite solar cells. *Energy Environ Sci* 2019; **12**: 2778–88.
- Caprioglio P, Wolff CM, Sandberg OJ *et al.* On the origin of the ideality factor in perovskite solar cells. *Adv Energy Mater* 2020; **10**: 2000502.
- Khenkin MV, Katz EA, Abate A *et al.* Consensus statement for stability assessment and reporting for perovskite photovoltaics based on ISOS procedures. *Nat Energy* 2020; **5**: 35–49.